Multi-interface superstructure strategy to improve the catalytic activity and cyclic stability in enhancing the photo conversion in solar cells

Jixin Yao[a,1], Wen Wang[a,1], Xueqin Zuo[a], Qun Yang[a], Muhammad Wasim Khan[a], Mingzai Wu[a,b], Huaibao Tang[a,b], Shaowei Jin[a,b], Guang Li[a,b,c,*]

[a] School of Physics and Materials Science, Anhui University, Hefei 230601, China
[b] Anhui Key Laboratory of Information Materials and Devices, Hefei 230601, China
[c] Institute of Physical Science and Information Technology, Anhui University, Hefei 230601, China

ABSTRACT

The development and design of counter electrode (CE) materials using an excellent catalytic activity and cyclic stability have a significant importance for further achieving better photoelectric conversion efficiency (PCE) of dye-sensitised solar cells (DSSCs). Achieving an efficient integration of ternary active components into the CEs and understanding the interaction between the ternary components are desired. Herein, a multistep transformation approach to constructing NiS nanosheets that are fixed on the surface of *N*-doped hollow thin shell carbon spheres (NHCS), and then encapsulated using reduced graphene oxide (RGO) to form an NHCS/NiS/RGO nanocomposite, is demonstrated. The nanocomposite shows an excellent electrochemical property and further probes the interfacial charge distribution behaviour as a CE for DSSCs. The interfacial charge polarisation with a large surface area of RGO facilitates a charge transfer, and evenly distributed NiS nanosheets on the surfaces of the NHCS gathering electrons lead to a strong interfacial coupling and simultaneously further boost the charge transfer, as well as triiodide oxidation and reduction, with remarkable ternary functional electrode activities. A device with an NHCS/NiS/RGO nanocomposite as a CE produces a better photovoltaic conversion efficiency (PCE) of up to 9.32% more than the Pt as a CE (8.06%). This study not only offers a strategy to achieving a ternary-functional-catalyst material with a superb performance, but also unravels the role of the geometric configuration factor of the hybrid from the view of the interfacial charge distribution, offering an abundant prospective roadmap of electrode materials in energy devices.

1. Introduction

In the 21st century, the energy structure is facing an important change in that the mineral energy system should be replaced with a renewable energy system, and this change is bringing about more intense research into renewable energy collection technologies [1–13]. Thus, searching for a low-cost, natural-resource rich, and easy-to-collect energy source should be an important start for renewable energy studies. Solar energy is the cleanest and most inexhaustible source of energy available, and has been favoured by many researchers [14–24]. Differing from current conventional solar cells, a comparatively lesser electron hole recombination rate can be achieved in dye-sensitised solar cells (DSSCs), of which the photoelectrons are respectively produced through photosensitive dyes and transferred using a semiconductor under sunlight irradiation [25–28]. Hence, a greater conversion

efficiency can be realised. DSSCs even generate electricity well under little sunlight intensity, which extends their application to indoor areas. In addition, DSSCs can synthesise a diverse morphology, as well as various colours and transparencies, allowing a wide range of requirements in various applications to be fulfilled [29].

A standard DSSC cell is made up of a transparent conductive optical glass, nanoporous electrode (TiO₂ photoanode), a counter electrode (photoelectric cathode) that operates in the dark, a dye, and an electrolyte [6,30–39]. Optical transparency is very important in certain practical applications, such as windows, roof panels, or various decorative installations. Transparent counter electrodes are essential for the operation of plastic DSSC and tandem solar cells. In solar cells with conductive glass applied as the photocathode substrate, the optical transparency of the counter electrode is unimportant to the function of the DSSC, but provides added value for the above practical applications

---

[39]. As an important part of a DSSC, the counter electrode has two functions: the first is to transfer the electrons back from the outside path to the redox system, and the second is to catalyse the reduction of iodide ions [40,41]. The I^- single-electron oxidation process ensures an effective regeneration of dyes; meanwhile, a reduction in the efficiency of I_3^- on the surface of an anode is relatively low. This asymmetric behaviour is the basis for the efficient operation of iodine-based DSSCs. A large specific surface area can facilitate a charge transfer, which can form a positive interaction and strengthen the overall electronic cycle, thereby promoting the catalytic performance during photoelectric conversion [42,43]. Hence, an ideal counter electrode (CE) material should ensure a better electrocatalytic activity and preeminent conductivity, excellent chemical stability, and low price [44–46]. In the field of counter electrode catalytic materials, Pt has been recognised as a reference electrode owing to its superb electrocatalytic capability. Nevertheless, because of the scarcity of natural reserves, Pt is significantly overpriced. Excessive costs and instability have generally made the mass production and marketable applications of DSSCs difficult to achieve [47–49]. Hollow structure materials are frequently used to promote the electrocatalytic performance [50–53]. Therefore, a hollow structure with diverse hierarchical architectures has attracted considerable interest owing to its wide use in energy conversion and storage, as well as several other fields [54–57]. However, an efficient integration of the carbon/metal/sulfide/carbon constituents and an exploration of the interaction of these components are infrequent. The development of synthesis stratagems with accurate structural controls and designs has been satisfactory, although the assembly of a highly efficient multicomponent catalyst electrode remains a challenge. To achieve an improved electrochemical performance of an advanced CE material for a DSSC, the design of the nanostructured composite materials should concentrate on the following aspects: (1) a uniform nanoscale structure facilitating a good transport of electrons, (2) a hollow hybrid nanostructure of electrocatalysts possessing superior electrocatalytic activities, (3) hierarchical porous materials with a high surface area maximising the absorption of electrons in the electrolyte, (4) a superior stability of nanocomposites in an electrolyte, and (5) a simple and low-cost strategy. However, it is difficult to accomplish each of the above requirements in a single CE.

Aiming at the significant problems described above, we constructed the reasonable design and controllable fabrication of a novel and highly uniform hollow hierarchical NHCS/NiS with a size of approximately 400 nm, and encapsulated with reduced graphene oxide (RGO) to form a unique ternary interfacial structure (NHCS/NiS/RGO composite). Heteroatom doping of hollow carbon spheres allows for more active catalytic sites. The porous NiS nanosheets grown on *N*-doped hollow carbon spheres ensure interconnected channels providing short electrolyte ion diffusion paths along different directions. When applied as a CE for DSSCs, a higher PCE of 8.78% than that of Pt (8.06%) was achieved. Once the RGO is successfully introduced in the wrapping of the NHCS/NiS, the ternary interfacial interactions of the NHCS/NiS/RGO composites enhance the catalytic performance and further boost the electronic adsorption and migration owing to its special layer structure. Hence, a much better PCE (9.32%) is achieved, which is also much more than that of Pt.

2. Results and discussion

The modified and optimised production process of the hierarchical NHCS/NiS/RGO nanocomposites of a hollow structure is illustrated in Scheme 1(a). First, NHCS/NiS/RGO was reasonably designed and synthesised using a multistep revolution method, which are clearly displayed in Step 1. Subsequently, the experimental steps were simplified and improved, as shown in Step 2. The synthesis roadmap of Step 2 is shown in Scheme 1(b). Initially, $NiCl_2$, NH_4Cl, $NH_3 \cdot H_2O$, and $CO(NH_2)_2$ were added into deionised water and stirred for 30 min., and SiO_2/*N*-carbon and Na_2S were then poured into this uniform mixture solution

with ultrasonic oscillation for 30 min. GO (250 mg) was obtained from XFNANO Materials Tech Co. Ltd. (100620, Nanjing, China), which was then dispersed in a mixture solution using ultrasonic oscillation for 60 min to form a homogeneous solution. The mixed solution was transferred into a Teflon-lined autoclave and heated at 160 °C for a chemical reaction. The sample was collected through centrifugation and washed several times with deionised water and subsequently dried in a freezer dryer for 1 day and annealed at 400 °C for 2 h in a N_2 atmosphere to form a NHCS/NiS/RGO composite. A 2D image, shown at the bottom-right of Scheme 1(b), is provided to intuitively illustrate the interface structure of a NHCS/NiS/RGO composite (see the Supporting Information for the experimental procedures and details).

The microstructures and morphology evolvements of NHCS/NiS and NHCS/NiS/RGO can be clearly recognised using scanning electron microscopy (SEM) and transmission electron microscopy (TEM) observations. Fig. 1 shows typical SEM images of NHCS/NiS and NHCS/NiS/RGO at different magnifications. As shown in Fig. 1a and b, the prepared NHCS/NiS forms 3D uniform hierarchical structures with a diameter of approximately 400 nm. Meanwhile, it is also clearly confirmed that the surface of NHCS/NiS is composed of interconnected nanosheets, which can supply higher specific surface areas, larger pore volumes, and a shorter route for ionic and electronic transport. It is noteworthy that NHCS/NiS is wrapped within the graphene layers and displayed in Fig. 1c and d, implying an efficient assembly between the NHCS/NiS and the graphene layers. Such a versatile sandwich structure is beneficial for application as a counter electrode for a DSSC, which is expected to effectively prevent the collapse of a hollow structure and impede the direct contact between the electrolyte and NiS, and thus will not be easily damaged.

TEM characterisation further confirmed the even distribution and uniform internal structure of the NHCS/NiS and NHCS/NiS/RGO nanocomposites. The high-magnification TEM images in Fig. 2a and b clearly show that NHCS/NiSi microspheres possess a uniform core shell structure. When the reaction time reached 12 h, the core of the SiO_2 was gradually eliminated to form a hollow structure, which is labelled as a precursor of the NHCS/NiS and then vulcanised to form an NHCS/NiS hierarchical hollow structure (Fig. 2c and d). It is noteworthy that the surface morphologies of NHCS/NiS are more abundant and complex than those of NHCS/NiSi, implying that NiS nanosheets grow completely on the surface of the NHCS to form a stable interfacial structure. This is ready to increase the contact area between the synthetic material and electrolyte, accelerating the effective ion transport in promoting the adsorption and desorption of the reactants. Furthermore, the hollow structure of the NHCS combining a NiS nanosheet shell with an RGO are further verified in Fig. 2e and f, which can offer rich electrochemical active sites and a larger electrolyte-electrode contact area for a I^-/I_3^- redox coupling reaction. Simultaneously, the *N*-doped carbon spheres further increase the electron transmission, which can improve the conductivity. In addition, the introduction of graphene can facilitate the electrolyte diffusion and penetration, thereby promoting the electrochemical activity and stability of the hybrids. Apart from these, an elemental mapping analysis for an NHCS/NiS/RGO sphere (Fig. 2g) demonstrates a uniform presence and distribution of Ni, S, C, N, and O elements in the NHCS/NiS/RGO nanocomposites, as shown in Fig. 2h–l. It is worth noting that N is uniformly distributed in the NHCS/NiS/RGO nanocomposites, signifying the idea that Ni–S–C–N active sites are definitely at the NiS interface [58–61]. The existing double carbon layers (RGO and NHCS) can protect the NiS nanosheets from excessive corrosion in an electrolyte; hence, a stable ternary interfacial structure was formed.

X-ray diffraction patterns (XRD) and X-ray photoelectron spectroscopy (XPS) were recorded to explore the crystal structure and composition of NHCS/NiSi, NHCS/NiS, and NHCS/NiS/RGO nanocomposites, as illustrated in Fig. 3. The crystal structures of NHCS, NHCS/NiS, and NHCS/NiS/RGO were determined based on the XRD patterns and are shown in Fig. 3a. The wide peak at 23.5° can be allocated to NHCS
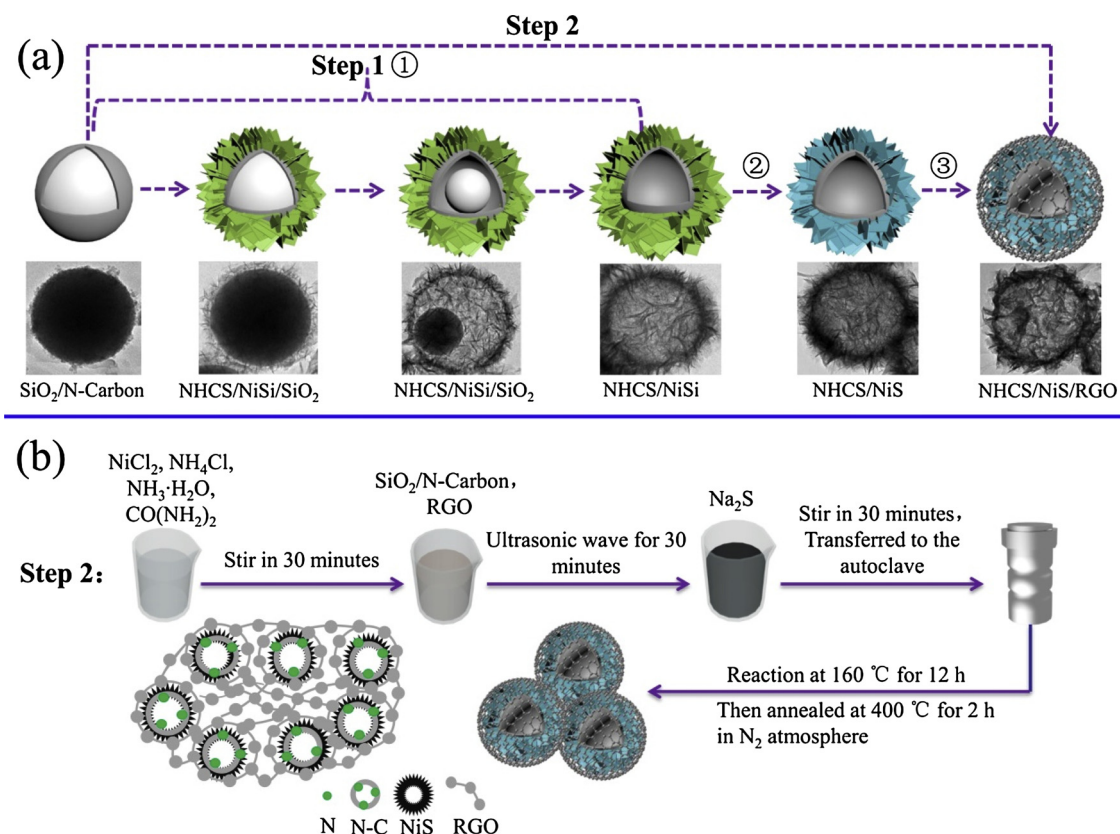
Scheme 1. (a) Two steps fabrication of the NHCS/NiS/RGO composites. The images in the top line are imagination maps, while the images in the bottom are the images recorded via TEM at different stages. (b) Synthetic routes of Step 2 for NHCS/NiS/RGO hybrid architecture.
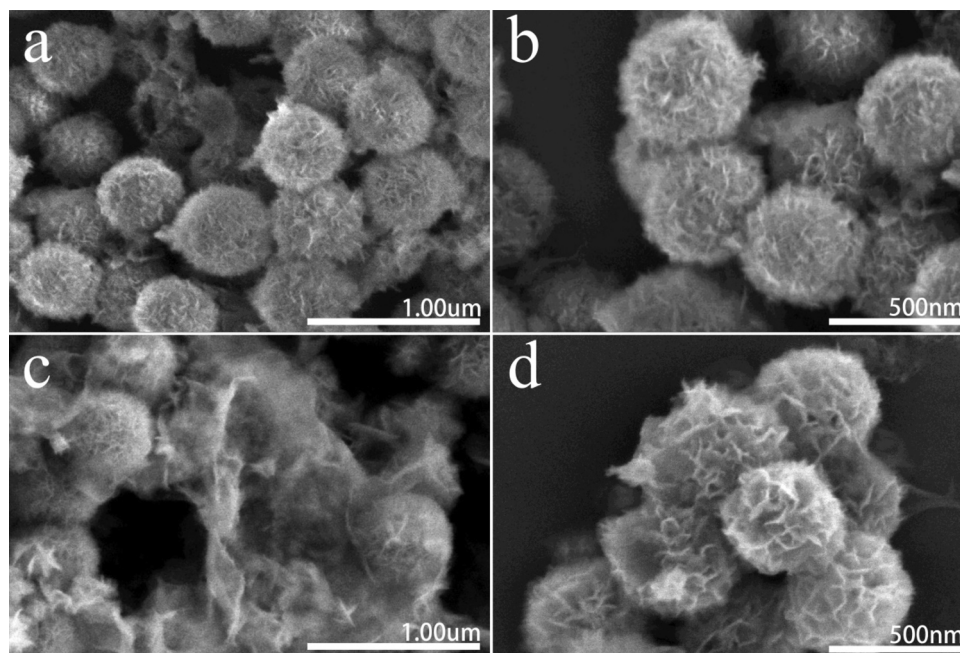

Fig. 1. (a) and (b) SEM images of NHCS/NiS, (c) and (d) SEM images of NHCS/NiS/RGO.

and RGO, signifying the characteristic defective structure. A series of peaks at 19.4°, 30.3°, 32.7°, 35.9°, 53.5°, and 59.8° are devoted to (110), (101), (300), (021), (401), and (012) crystal planes of NiS (JCPDF, 86–2281), respectively [62], demonstrating the NiS component inside the achieved samples.

The Raman spectroscopy of NHCS, NHCS/NiS, and NHCS/NiS/RGO nanocomposites display two main peaks at 1348 and 1595 cm^{-1} distributed to typical D and G bands [63–65], which are shown in Fig. S5. The intensity ratio of the D and G bands can be used to evaluate the defect density of the carbon materials. It is worth noting that a higher I_D/I_G ratio for NHCS/NiS suggests more inner defective sites [64]. NHCS/NiS/RGO nanocomposites possess a lower I_D/I_G ratio, which
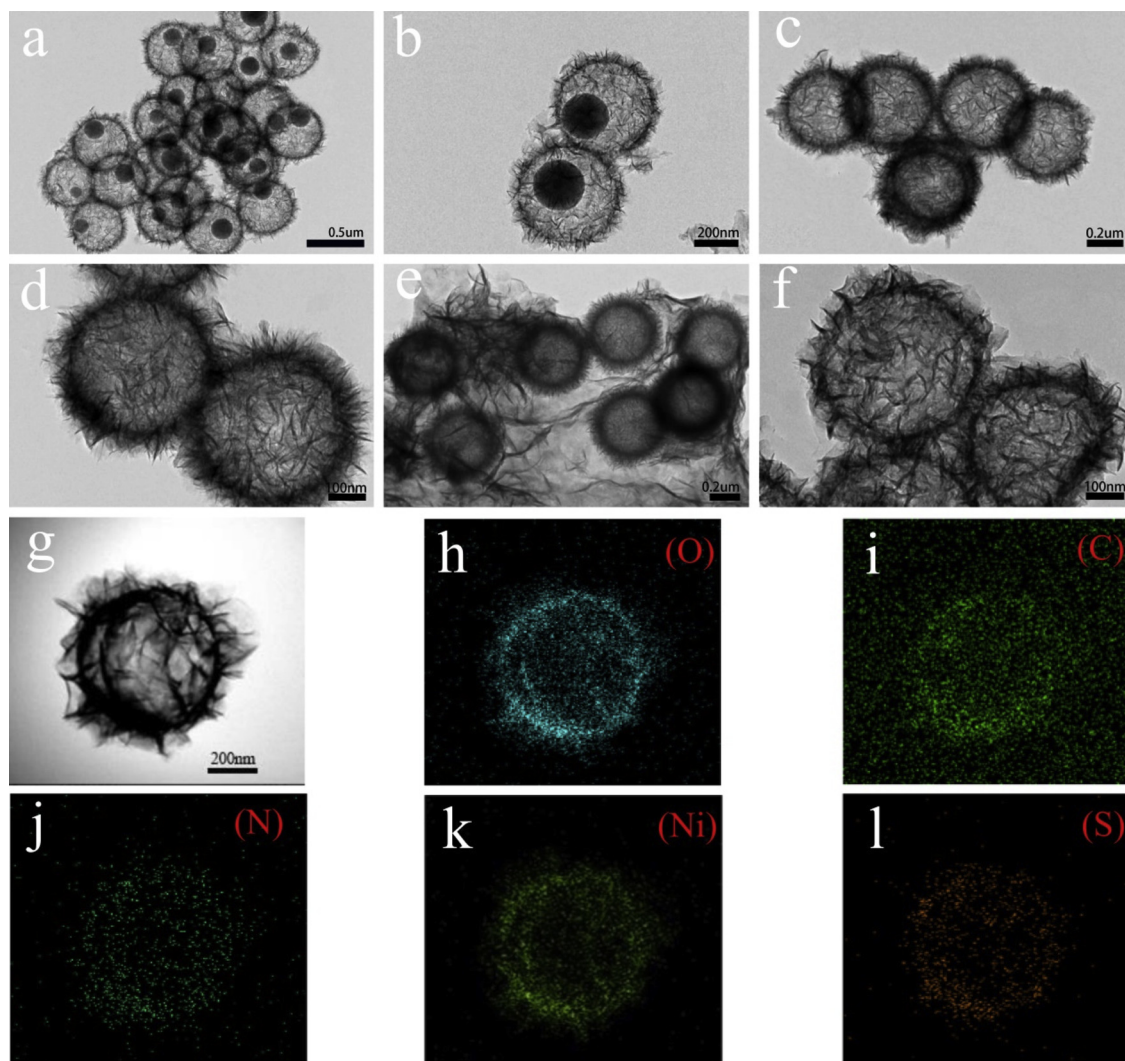
Fig. 2. (a and b) TEM images of NHCS/NiSi with a reaction time of 8 h, in which the solid sphere/core is SiO$_2$. (c and d) TEM micrographs of NHCS/NiS. (e and f) TEM micrographs of NHCS/NiS/RGO. STEM image taken from the square region marked in (g). (c–f) Corresponding elemental mapping images of (h) O element, (I) C element, (j) N element, (k) Ni element, (l) S element.

may be caused by the Raman spectra focusing only on the RGO. In addition, the presence of an RGO has been shown through SEM and TEM.

Furthermore, the relevant element components of NHCS/NiS/RGO nanocomposites are further verified through XPS detections. Fig. 3b shows that NHCS/NiSi, NHCS/NiS, and NHCS/NiS/RGO nanocomposites contain signals of different elements. It is clear that the NHCS/NiSi nanocomposites have silicon, carbon, oxygen, nitrogen, and nickel. NHCS/NiS and NHCS/NiS/RGO nanocomposites contain sulfur, carbon, oxygen, nitrogen, and nickel. The chief peaks of Fig. 3c corresponding to Ni 2p$_{3/2}$ and Ni 2p$_{1/2}$ are placed at 854.2 and 872.2 eV, and two shake-up satellites are placed at 880.5 and 861.2 eV; in addition, the Ni 2p$_{3/2}$ peak of Ni^{3+} is located at 856.1 eV and 874.3 eV, and that of Ni^{2+} is centred at 854.2 eV and 872.1 eV [66].

In Fig. 3d, the N1s XPS spectra are divided into four types, which can be allocated to pyridinic N, pyrrolic N, quaternary N, and oxidised pyridinic N, whose main peaks are located at 398.8, 399.4, 400.3, and 403.2 eV, respectively, indicating the existence of N doping in a spherical hollow carbon structure [67,68]. Fig. 3e demonstrates the S2p XPS spectrum for a NHCS/NiS/RGO nanocomposite with two binding energy peaks at 163.1 and 164.2 eV, and corresponds to S2p$_{3/2}$ and S2p$_{1/2}$ energies of S^{2-} in the NHCS/NiS/RGO nanocomposites, respectively [62]. In addition, another peak at 168.4 eV belongs to sulfur oxide from

the oxidation of S with residual O$_2$. Finally, as shown in Fig. 3f, the high-resolution spectrum of C1s can be separated into four peaks, corresponding to C=C (284.8 eV), C−N (285.2 eV), C−O (286.5 eV), and C=O (287.5 eV). The existence of C−N may be derived from the interfaces between NiS and the carbon sphere matrix. More defects are from the introduction of heteroatom (N) used to modify the electronic structure of the RGO layers, which enhances the material conductivity, which can therefore accelerate the reduction of I$_3^-$ [69].

The specific surface area is a very significant factor in the entire catalytic process, which can directly affect the electron adsorption and transmission. A large specific surface area helps the materials boost the catalytic intensity and is also conducive to the rapid transfer of electrons, accelerating the catalytic speed [70]. The changes in N adsorption and desorption of the NHCS, NHCS/NiS, and NHCS/NiS/RGO samples are presented in Fig. 3g–i. As the figures indicate, NHCS spheres present a large specific surface area (750 m^2 g^{-1}) with a uniform hollow spherical framework; in addition, the specific surface area of the NHCS/NiS nanocomposites, *i.e.* the NiS nanosheets anchored on the surface of the NHCS, is approximately 316 m^2 g^{-1}, and the specific surface area of the NHCS/NiS/RGO nanocomposite is approximately 366 m^2 g^{-1}, which is higher than that of the NHCS/NiS nanocomposite. The pore size distributions were assessed using Barrett-Joyner-Halenda, which are exhibited in the inserts of Fig. 3g–i. The pore size distribution
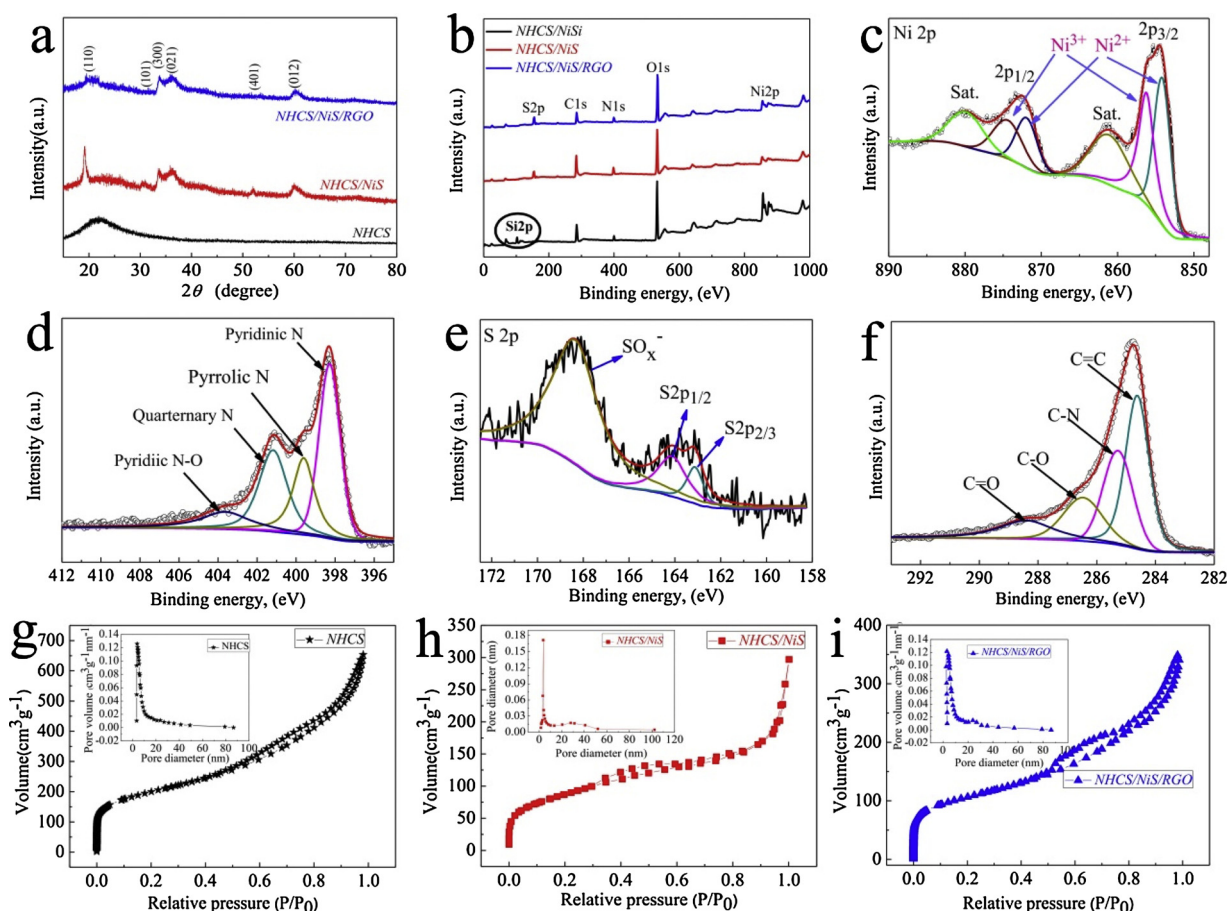
Fig. 3. (a) XRD patterns of NHCS, NHCS/NiS and NHCS/NiS/RGO. (b) Wide XPS spectra of NHCS/NiSi, NHCS/NiS and NHCS/NiS/RGO. (c) Ni2p spectra. (d) N1s spectra. (e) S2p spectra. (f) C1s spectra. (g–i) N_2 adsorption-desorption isotherms and corresponding pore size distribution of NHCS, NHCS/NiS, and NHCS/NiS/RGO.

is approximately 3.86, 6.86, and 5.42 nm, respectively. The functional integration of a hollow carbon spherical framework with NiS and RGO forms a sandwich structure, which might be used as a CE with an excellent catalytic performance because a large specific surface area allows the penetration of I^-/I_3^- and produces a rather high distribution of iodide ions, efficiently promoting electronic transport [71]. This specific performance can be analysed through an electrochemical test.

The schematic structure of a symmetric cell with two identical electrodes (CE/electrolyte/CE) is displayed in Fig. 4a, and used to evaluate the electron transfer process between the electrolyte and CE interface, as well as the data on the exchange current density through electrochemical impedance spectroscopy (EIS) and Tafel polarisation measurements [72,73]. Two remarkable semicircles are clearly presented in the Nyquist plot shown in Fig. 4b. The corresponding equivalent circuit is shown in the insert of Fig. 4b. The high-frequency intercept on the real axis is equal to the series resistance (R_S) for the entire cell. The height-frequency array is ascribed to the charge transfer resistance (R_{ct}) and the redox process at the counter electrode (CE)/electrolyte interface, which may be located in the left semicircles [74]. In addition, the right semicircle is the low-frequency range and mirrors the Nernst diffusion impedance (Z_N) of the redox couple transport in the electrolyte [75,76]. It is extremely important for DSSCs to assess faster reaction kinetics and an enhanced electrical conductivity with small values of R_{ct}, R_s, and Z_N of a CE/catalyst. The electrical conductivity of NHCS/NiS/RGO is remarkably higher than that of NHCS, NHCS/NiS, and Pt, suggesting that NHCS/NiS/RGO should possess a higher electrical conductivity, which can be reflected by the smaller value of R_s. Typically, R_{ct} is considered as another vital point disclosing the charge transfer process and allowing the catalytic activity of the CE to be estimated. The electron transmission from the CE to the electrolyte for a

catalytic reduction of I_3^- and the lesser interfacial reorganisation are investigated based on the R_{ct} value. Hence, the most outstanding value is shown for NHCS/NiS/RGO as compared to that of NHCS, NHCS/NiS, and Pt. The parameters R_s and R_{ct} for all CEs are listed in Table 1. Notably, NHCS offers a hollow interior, which promotes the diffusion of I_3^- [77,78]. The NHCS/NiS/RGO hybrids show that electrons will migrate from the NiS to the RGO layer owing to the strong interfacial polarisation between them [79]. Subsequently, the rapid transfer of electrons is due to the synergistic effect of the special construction of graphene and NHCS/NiS.

Tafel polarisation curves were executed to further clarify the catalytic activity for movement across the electrode surface of the I^-/I_3^- redox couple for these CEs in DSSCs [80]. The Tafel curves from various CEs are shown in Fig. 4c. The polarisation area, Tafel area, and diffusion area should also provide an important reference to the catalytic activity. In fact, the exchange current density (J_0) and limiting diffusion current density (J_{lim}) correspond to the Tafel and diffusion zones, respectively, which can be applied to estimate the catalytic activity of different CEs for an I_3^- reduction [81]. Furthermore, the Tafel zone is defined by the slope of the cathode branch. Here, J_0 and J_{lim} can be obtained by deducing the Tafel curves; J_0 reveals the catalytic activity of the CE material and electrolyte, and J_{lim} is a crucial parameter for estimating the efficiency of a DSSC. The values of J_0 and J_{lim} are clearly shown in Table 1, and can be acquired through Eqs. (1) and (2).

$$J_0 = \frac{RT}{nFR_{ct}} \tag{1}$$

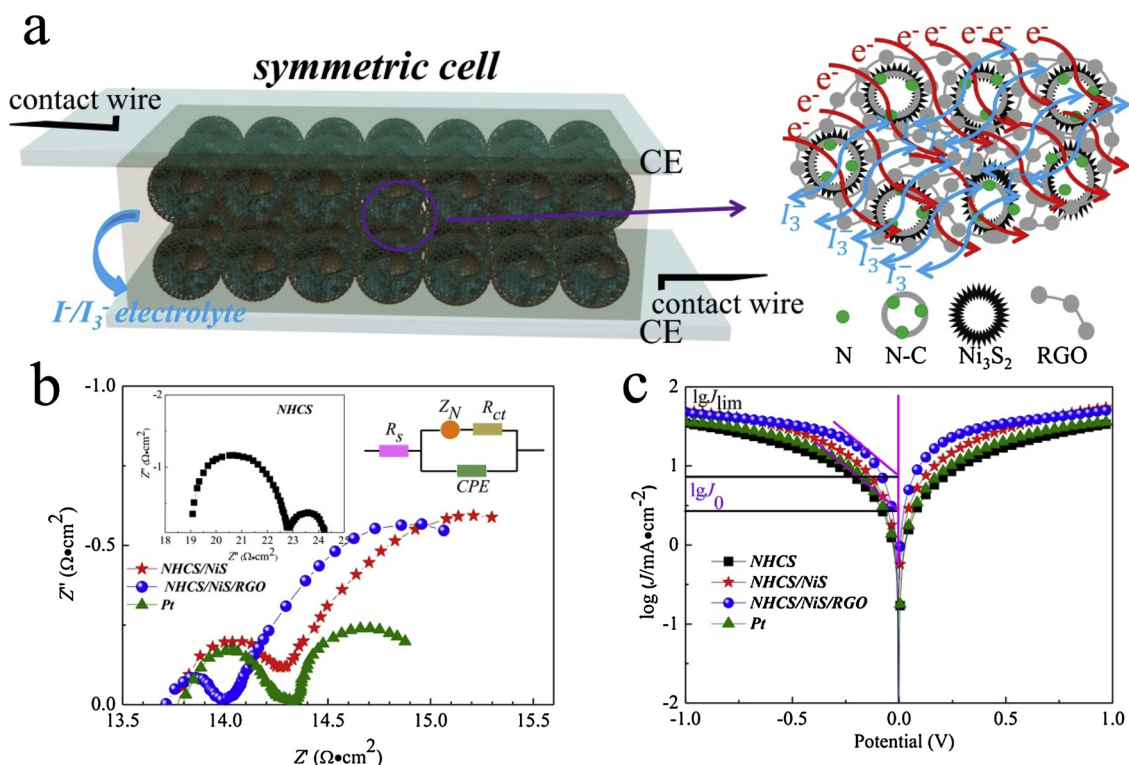$$J_{lim} = \frac{2neDCN_A}{l} \tag{2}$$

Fig. 4. (a) Schematic structure of a symmetric cell used for the measurement of Tafel polarisation and EIS. Two-dimensional graph displays electrons' movements. (b) Nyquist plots of DSSCs using Pt thin film, NHCS, NHCS/NiS, and NHCS/NiS/RGO as the CE. (c) Tafel polarisation curves of the Pt thin film and NHCS, NHCS/NiS, and NHCS/NiS/RGO nanostructures.

Table 1
Parameters derived from EIS and Tafel curves recorded under the same environment for DSSCs equipped with CEs made of NHCS, NHCS/NiS, NHCS/NiS/RGO.

CEs	R_s ($\Omega\,cm^2$)	R_{ct} ($\Omega\,cm^2$)	lgJ_0 (mA cm^{-2})	lgJ_{lim} (mA cm^{-2})	E_{PP} (V)
NHCS	19.1	1.88	0.44	1.51	0.35 ± 0.01
NHCS/NiS	13.8	0.25	0.73	1.67	0.28 ± 0.01
NHCS/NiS/RGO	13.7	0.14	0.87	1.69	0.25 ± 0.01
Pt	13.8	0.27	0.56	1.54	0.34 ± 0.01

For the detailed meanings of the parameters, refer to the Supporting Information.

In a DSSC, cyclic voltammogram (CV) measurements are conducted to immediately examine the reaction kinetics and electro-catalytic activities of the various CEs with a redox reduction of I_3^- in the electrolyte [82]. The principle diagram is shown in Fig. 5a, which clearly describes the functions of CE, i.e. adsorption, dissociation, and desorption for iodide ions. Clearly, the CV curves in Fig. 5b show two pairs of oxidation and reduction peaks, which can be allocated to Ox1/Red1 and Ox2/Red2, and achieved in a three-electrode system with a step of 25 mV s^{-1}. The principle of a catalytic reaction in an iodide ion is exposed by oxidation and reduction peaks (Ox1/Red1 and Ox2/Red2). Eqs. (3) and (4) are employed to explain the circular reaction of the entire CE interface for an I^-/I_3^- redox.

$$I_3^- + 2e^- = 3I^- \tag{3}$$

$$3I_2 + 2e^- = 2I_3^- \tag{4}$$

The peaks of Ox1 and Red1 are generally more noteworthy than those of Ox2 and Red2 because the emergence of the peaks for Ox1 and Red1 is due to the redox reaction of I^-/I_3^-, whereas those of Ox2 and Red2 are associated with the oxidation and reduction of I_3^-/I_2 on the surface. Meanwhile, the peak intensity of Ox1 and Red1 can be reflected by the current density, which is mainly revealed in the adsorption and transfer of ions on the surface of the CE materials and is an important factor in assessing the current density for iodide ions [83]. It is worth mentioning that the values of the peak intensity (Ox1 and Red1) are in the order of NHCS < Pt < NHCS/NiS < NHCS/NiS/RGO, as presented in Fig. 5c and d, suggesting the outstanding adsorption of NHCS/NiS/RGO for electrons, which is superior to that of Pt. The gap between Ox1 and Red1 is labelled as E_{pp}, and is clearly shown in Fig. 5e. A narrower distance for E_{pp} indicates much higher catalytic speeds for an I^-/I_3^- redox in the CEs. The E_{pp} of NHCS/NiS/RGO is 0.26 V, and that of NHCS/NiS is 0.28 V, which are much lower than that of Pt (0.35 V), demonstrating that electrons can be rapidly transferred to promote the mutual transformation of iodide ions. An excellent conductivity and catalytic performance may be attributed to the synergistic effects and structural integration between carbon materials and metal sulfides, and the intimate interfacial connections through abundant N−C−Ni−S−C bonds [84].

Fig. 6a shows the working principle of an entire cell with a sandwiched structure to test the photoelectric conversion performance of various CEs. The photocurrent density–voltage (J–V) curves of the as-prepared samples are irradiated at AM 1.5 (100 mW cm^{-2}), as shown in Fig. 6b. The correlative data parameters for the J–V curves are shown in Table 2. These PCE results are clearly shown in Fig. 6c. NHCS/NiS/RGO attains a higher PCE (9.32%) than NHCS (5.05%), NHCS/NiS (8.78%) and Pt (8.06%), which can be attributed to a higher J_{sc} (22.3 mA cm^{-2}) and V_{oc} (0.773 V) and a smaller R_{ct}, the former of which has a smaller FF (54.07%).
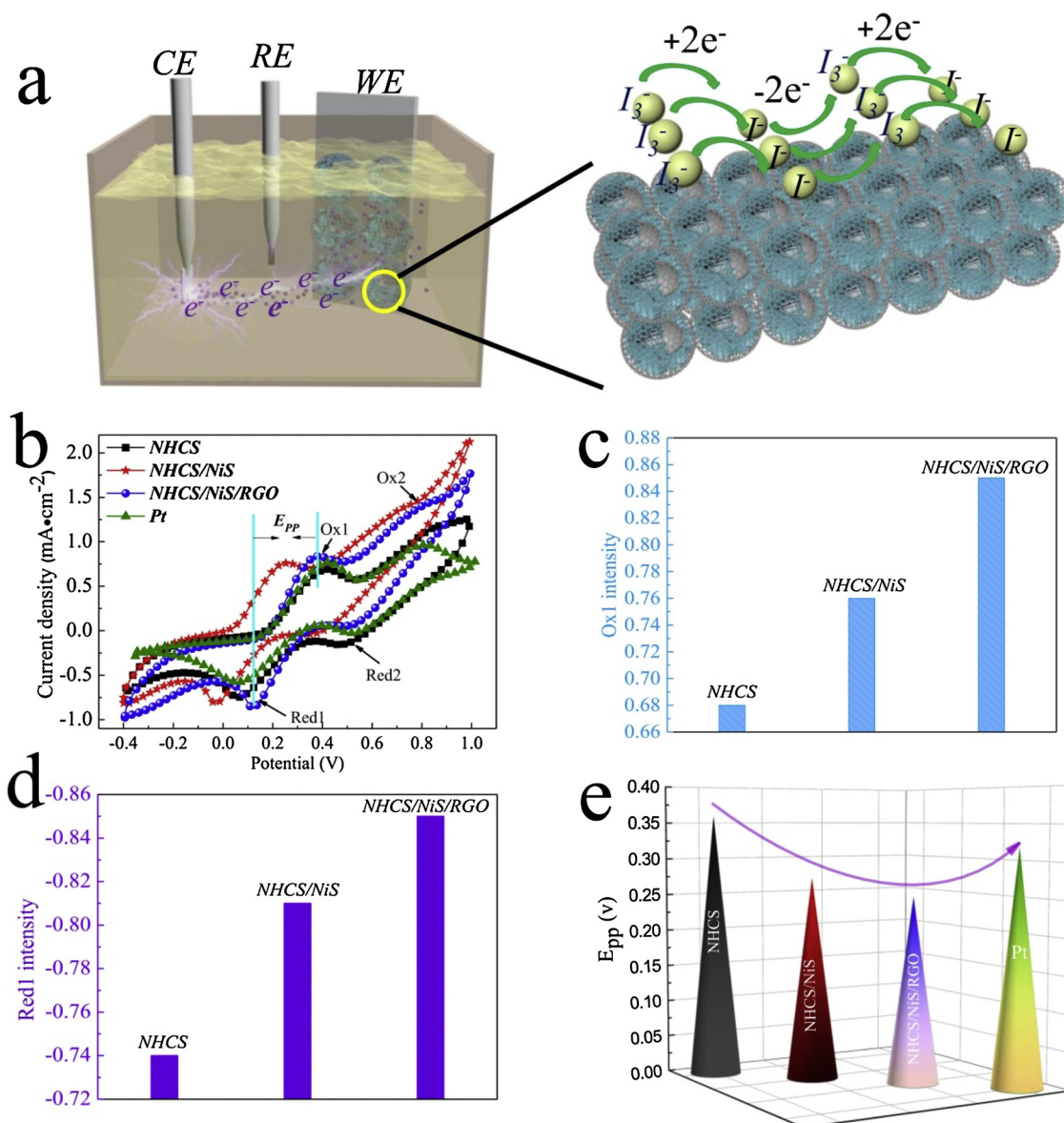
Fig. 5. (a) Schematic diagram of I_2 in NHCS/NiS/RGO adsorption, dissociation, and desorption during CV measurement. (b) Cyclic voltammograms of the Pt, NHCS, NHCS/NiS, and NHCS/NiS/RGO nanostructures for the redox of I^-/I_3^- species. (c) Ox1 intensity. (d) Red1 intensity. (e) Cyclic voltammograms of E_{pp} for all samples and Pt.

The IPCE curves of the developed DSSCs with all CEs were determined and are shown in Fig. 6d. The wavelength of the IPCE spectra ranges from 450 to 700 nm, signifying a related photo-electric response. Notably, the highest photo-response of 78% for NHCS/NiS/RGO CE-based DSSCs is more than that of NHCS/NiS (72%), NHCS (70%), and conventional Pt (64%). The photo-response of these CE-based DSSCs is related to their J_{sc} values. Furthermore, these results agree with the EIS, CV, and $J–V$ analyses, indicating that the NHCS/NiS/RGO nanocomposites may be replaceable counter electrodes for Pt in a DSSC.

The electrochemical stability is another important evaluation parameter for a DSSC. The stability of the as-prepared CEs was checked through CV tests for 30 cycles using an identical scanning rate (25 mV/ s), the results of which are shown in Fig. S7. Clearly, the NHCS/NiS/ RGO nanocomposites have a superb stability, and their performances exceed that of a conventional Pt. Moreover, after the 30-cycle CV tests, the NHCS/NiS/RGO nanocomposites were tested for the $J–V$ curve again, as shown in Fig. S8. The power conversion efficiency of NHCS/ NiS/RGO reaches 8.68%, which can maintain approximately 93% of the original value. The morphology and structure of the NHCS/NiS/RGO

after corrosion were also observed through TEM, as indicated in Fig. S8.

All results reveal and confirm the steadily upgraded photoelectric conversion capability of CEs from NHCS to NHCS/NiS/RGO. The continuous enhancement in performance can be attributed to the following reasons and is vividly illustrated in Fig. 6e. In the conceptual diagram, CE materials provide electrons to I_3^- at the interface, which is of utmost importance for electron collection and transmission [76,85]. To begin with, NHCS is established as the basic framework for the entire CE material. It not only offers a large specific surface area, but also reveals the characteristics of an N species for an I_3^- reduction. Subsequently, NiS nanosheets are anchored to the surface of the NHCS, which enhances the contact area between the NHCS/NiS and the electrolyte. Furthermore, an RGO is introduced to wrap the NHCS/NiS and expand the exchange current between the NHCS/NiS/RGO and electrolyte, accelerating the charge transfer. More specifically, the diffusion speeds reach the peak for the charges and ions. Such a progressively and steadily upgraded photoelectric conversion capability of the CEs from NHCS to NHCS/NiS/RGO can be presented visually using a bicycle, car, and high-speed train (please refer to the conceptual diagram of
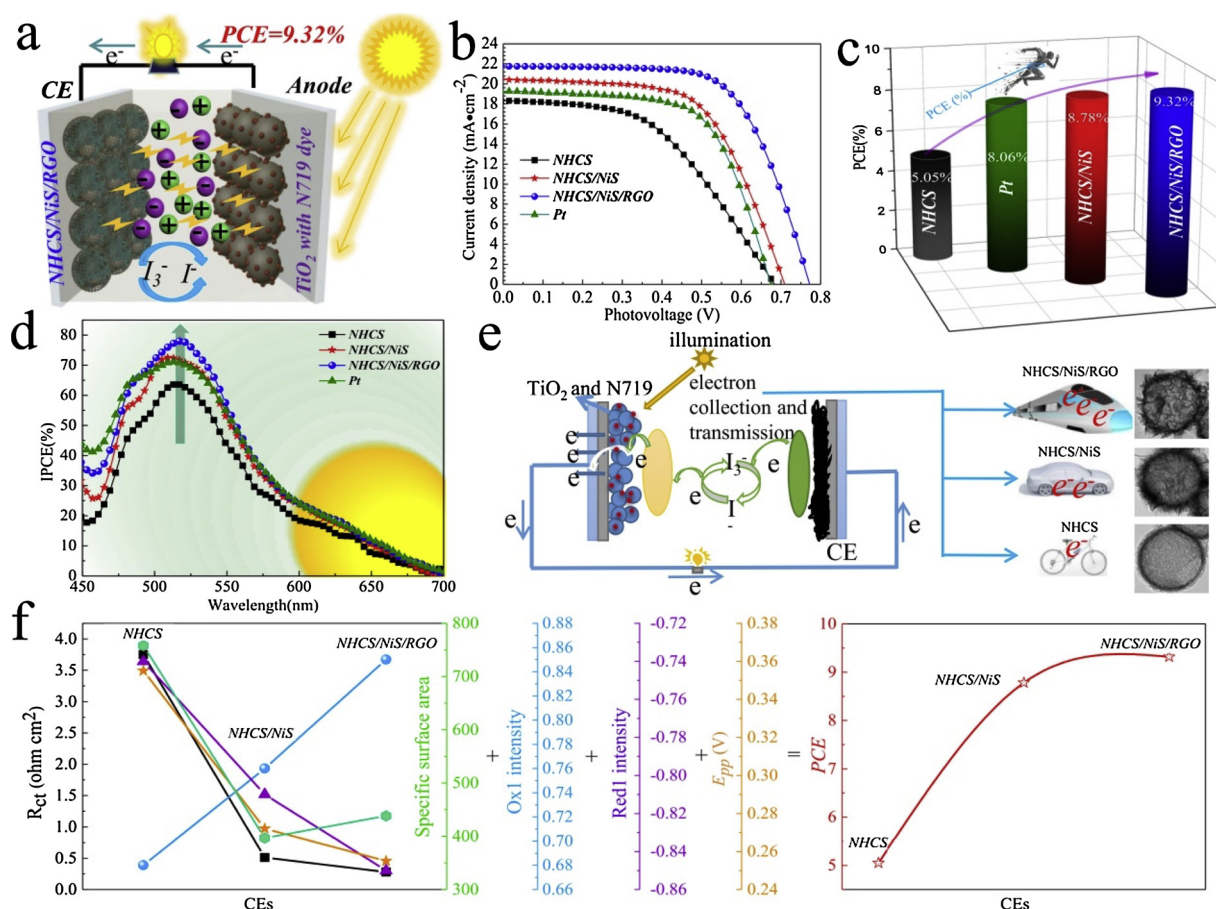
Fig. 6. (a) Schematic structure of a DSSC using NHCS/NiS/RGO as the CE to form a full cell. (b) J–V curves of DSSCs with different CEs. (c) The value of PCE for all samples including a DSSC with the CE made of Pt. (d) IPCE curves of DSSCs with different CEs. (e) A conceptual diagram of structural change effects on electronic transportation. (f) The variation value of R_{ct}, specific surface area, Ox1 intensity, Red1 intensity and E_{pp} and the relevance of PCE of DSSCs equipped with different CEs.

Table 2

Photovoltaic parameters for DSSCs recorded under the same environment for DSSCs equipped with CEs made of NHCS, NHCS/NiS, NHCS/NiS/RGO.

CEs	J_{SC} (mA cm^{-2})	V_{OC} (V)	FF (%)	PEC (%)
NHCS	18.3	0.688	41.31	5.05%
NHCS/NiS	20.4	0.773	55.67	8.78%
NHCS/NiS/RGO	22.3	0.773	54.07	9.32%
Pt	19.3	0.673	62.05	8.06%

structural change effects on electronic transportation on the right side of Fig. 6e).

Herein, all relevant data such as R_{ct}, the specific surface area, Ox1 intensity, Red1 intensity, and E_{pp}, which have a significant impact on the value of PCE of the DSSC, along with the as-prepared CEs are displayed in Fig. 6f. It is notable that the variation trends of the value R_{ct}, Red1 intensity, and E_{pp} are the same, which are an inverse of the Ox1 intensity of the CV curve. Moreover, the specific surface area is extremely unique, decreasing and then increasing. This is due to the introduction of N atoms, which improves the catalytic activity of spherical hollow carbon substrates, the conductivity of which does not achieve an optimal state. Hollow carbon spheres offer a specific surface area, and metal sulfide enhances the conductivity and catalytic activity for the complexes, providing synergy between them. The RGO further enlarges the specific surface area of the composites, facilitating the absorption and rapid transfer of more electrons, thereby enhancing the catalytic strength and speeding up the catalytic reaction. Finally, the optimal performance is realised in the sandwich structure of NHCS/ NiS/RGO.

3. Conclusions

We demonstrated the use of NHCS as a substrate to prepare the functional sandwich structure of NHCS/NiS/RGO nanocomposites for a DSSC application. Electrochemical tests prove that the NHCS/NiS/RGO nanocomposite exhibits better catalytic activities than NHCS, NHCS/ NiS, or Pt, signifying the indispensable roles of a multi-interface superstructure affecting the electronic modulation from the interfacial charge redistribution. Such a nanocomposite possesses the potential to boost the development of correlated energy technologies and devices.

Acknowledgments

Appendix A. Supplementary data

Supplementary material related to this article can be found, in the online version, at doi:https://doi.org/10.1016/j.apcatb.2019.117857.

References

[1] F. Yu, Y. Shi, X. Shen, W. Yao, S. Han, J. Ma, Three-dimensional MoS$_2$-nanosheet-based graphene/carbon nanotube aerogel as a Pt-Free counter electrode for high-efficiency dye-sensitized solar cells, ACS Sustain. Chem. Eng. 6 (2018) 17427–17434.

[2] Q. Tang, W. Zhu, B. He, P. Yang, Rapid conversion from carbohydrates to large-scale carbon quantum dots for all-weather solar cells, ACS Nano 11 (2017) 1540–1547.

[3] M. Liu, M.B. Johnston, H.J. Snaith, Efficient planar heterojunction perovskite solar cells by vapour deposition, Nature 501 (2013) 395–398.

[4] Y. Kim, K. Bicanic, H. Tan, O. Ouellette, B.R. Sutherland, F.P. Garcia de Arquer, J.W. Jo, M. Liu, B. Sun, M. Liu, S. Hoogland, E.H. Sargent, Nanoimprint-transfer-Patterned solids enhance light absorption in colloidal quantum dot solar cells, Nano Lett. 17 (2017) 2349–2353.

[5] M. Ye, X. Wen, M. Wang, J. Iocozzia, N. Zhang, C. Lin, Z. Lin, Recent advances in dye-sensitized solar cells: from photoanodes, sensitizers and electrolytes to counter electrodes, Mater. Today 18 (2015) 155–162.

[6] J. Briscoe, S. Dunn, The future of using earth-abundant elements in counter electrodes for dye-sensitized solar cells, Adv Mater 28 (2016) 3802–3813.

[7] L. Yang, X. Wang, X. Mai, T. Wang, C. Wang, X. Li, V. Murugadoss, Q. Shao, S. Angaiah, Z. Guo, Constructing efficient mixed-ion perovskite solar cells based on TiO$_2$ nanorod array, J. Colloid Interface Sci. 534 (2019) 459–468.

[8] K. Le, Z. Wang, F. Wang, Q. Wang, Q. Shao, V. Murugadoss, S. Wu, W. Liu, J. Liu, Q. Gao, Z. Guo, Sandwich-like NiCo Layered Double hydroxide/reduced Graphene Oxide Nanocomposite Cathodes for High Energy Density Asymmetric Supercapacitors, Dalton Transactions, 2019.

[9] R. Li, X. Zhu, Q. Fu, G. Liang, Y. Chen, L. Luo, M. Dong, Q. Shao, C. Lin, R. Wei, Z. Guo, Nanosheet-based Nb$_{12}$O$_{29}$ hierarchical microspheres for enhanced lithium storage, Chem. Commun. (Camb.) 55 (2019) 2493–2496.

[10] R. Ge, S. Wang, J. Su, Y. Dong, Y. Lin, Q. Zhang, L. Chen, Phase-selective synthesis of self-supported RuP films for efficient hydrogen evolution electrocatalysis in alkaline media, Nanoscale 10 (2018) 13930–13935.

[11] B. Kirubasankar, V. Murugadoss, J. Lin, T. Ding, M. Dong, H. Liu, J. Zhang, T. Li, N. Wang, Z. Guo, S. Angaiah, In situ grown nickel selenide on graphene nanohybrid electrodes for high energy density asymmetric supercapacitors, Nanoscale 10 (2018) 20414–20425.

[12] Q. Hou, J. Ren, H. Chen, P. Yang, Q. Shao, M. Zhao, X. Zhao, H. He, N. Wang, Q. Luo, Z. Guo, Synergistic hematite-fullerene electron-extracting layers for improved efficiency and stability in perovskite solar cells, ChemElectroChem 5 (2018) 726–731.

[13] M. Liu, Z. Yang, H. Sun, C. Lai, X. Zhao, H. Peng, T. Liu, A hybrid carbon aerogel with both aligned and interconnected pores as interlayer for high-performance lithium-sulfur batteries, Nano Res. 9 (2016) 3735–3746.

[14] X. Liu, K. Yan, D. Tan, X. Liang, H. Zhang, W. Huang, Solvent engineering improves efficiency of lead-free tin-based hybrid perovskite solar cells beyond 9%, ACS Energy Lett. 3 (2018) 2701–2707.

[15] A. Bansal, H. Liu, M.K. Jayakumar, S. Andersson-Engels, Y. Zhang, Quasi-continuous wave near-infrared excitation of upconversion nanoparticles for optogenetic manipulation of C. Elegans, Small 12 (2016) 1732–1743.

[16] P. Zhao, Y. Zhu, X. Yang, X. Jiang, J. Shen, C. Li, Plasmon-enhanced efficient dye-sensitized solar cells using core–shell-structured β-NaYF4:Yb,Er@SiO2@Au nano-composites, J. Mater. Chem. A Mater. Energy Sustain. 2 (2014) 16523–16530.

[17] J. Zhou, Z. Liu, F. Li, Upconversion nanophosphors for small-animal imaging, Chem. Soc. Rev. 41 (2012) 1323–1349.

[18] C. Hou, Z. Tai, L. Zhao, Y. Zhai, Y. Hou, Y. Fan, F. Dang, J. Wang, H. Liu, High performance MnO@C microcages with a hierarchical structure and tunable carbon shell for efficient and durable lithium storage, J. Mater. Chem. A 6 (2018) 9723–9736.

[19] H. Chen, T. Liu, B. Wang, Z. Liu, Y. Li, Q. Zhao, N. Wang, H. He, H. Liu, Z. Guo, Highly efficient charge collection in dye-sensitized solar cells based on nanocomposite photoanode filled with indium-tin oxide interlayer, Adv. Compos. Hybrid Mater. 1 (2018) 356–363.

[20] M.M. Tavakoli, D. Prochowicz, P. Yadav, R. Tavakoli, M. Saliba, Zinc stannate nanorod as an electron transporting layer for highly efficient and hysteresis-less perovskite solar cells, Eng. Sci. 3 (2018) 48–53.

[21] Q. Jiang, L. Wang, C. Yan, C. Liu, Z. Guo, N. Wang, Mesoporous TiO$_2$ vacancies modification for halide perovskite solar cells, Eng. Sci. 1 (2018) 64–68.

[22] P. Panneerselvam, V. Murugadoss, V. Elayappan, N. Lu, Z. Guo, S. Angaiah, Influence of anti-reflecting nature of MgF$_2$ embedded electrospun TiO$_2$ nanofibers based photoanode to improve the photoconversion efficiency of DSSC, Synth. Lect. Energy Environ. Technol. Sci. Soc. 1 (2018) 99–105.

[23] R. Ge, X. Ren, X. Ji, Z. Liu, G. Du, A.M. Asiri, X. Sun, L. Chen, Benzoate anion-intercalated layered cobalt hydroxide nanoarray: an efficient electrocatalyst for the oxygen evolution reaction, ChemSusChem 10 (2017) 4004–4008.

[24] Q. Luo, H. Ma, Q. Hou, Y. Li, J. Ren, X. Dai, Z. Yao, Y. Zhou, L. Xiang, H. Du, H. He, N. Wang, K. Jiang, H. Lin, H. Zhang, Z. Guo, All-carbon-Electrode-Based endurable flexible perovskite solar cells, Adv. Funct. Mater. 28 (2018).

[25] J. Yao, K. Zhang, W. Wang, X. Zuo, Q. Yang, H. Tang, M. Wu, G. Li, Remarkable

[26] enhancement in the photoelectric performance of uniform flower-like mesoporous Fe$_3$O$_4$ wrapped in nitrogen-doped graphene networks, ACS Appl. Mater. Interfaces 10 (2018) 19564–19572.

[26] H. Huang, R. Cao, S. Yu, K. Xu, W. Hao, Y. Wang, F. Dong, T. Zhang, Y. Zhang, Single-unit-cell layer established Bi$_2$WO$_6$ 3D hierarchical architectures: efficient adsorption, photocatalysis and dye-sensitized photoelectrochemical performance, Appl. Catal. B 219 (2017) 526–537.

[27] H. Wang, K. Sun, F. Tao, D.J. Stacchiola, Y.H. Hu, 3D honeycomb-like structured graphene and its high efficiency as a counter-electrode catalyst for dye-sensitized solar cells, Angew. Chem. Int. Ed 52 (2013) 9210–9214.

[28] I.P. Liu, W.H. Lin, C.M. Tseng-Shan, Y.L. Lee, Importance of compact blocking layers to the performance of dye-sensitized solar cells under ambient light conditions, ACS Appl. Mater. Interfaces 10 (2018) 38900–38905.

[29] L. Chen, W.L. Chen, X.L. Wang, Y.G. Li, Z.M. Su, E.B. Wang, Polyoxometalates in dye-sensitized solar cells, Chem. Soc. Rev. 48 (2019) 260–284.

[30] P.-J. Chang, K.-Y. Cheng, S.-W. Chou, J.-J. Shyue, Y.-Y. Yang, C.-Y. Hung, C.-Y. Lin, H.-L. Chen, H.-L. Chou, P.-T. Chou, Tri-iodide reduction activity of shape- and composition-controlled PtFe nanostructures as counter electrodes in dye-sensitized solar cells, Chem. Mater. 28 (2016) 2110–2119.

[31] E. Bi, H. Chen, X. Yang, W. Peng, M. Grätzel, L. Han, A quasi core–shell nitrogen-doped graphene/cobalt sulfide conductive catalyst for highly efficient dye-sensitized solar cells, Energy Environ. Sci. 7 (2014) 2637–2641.

[32] X. Chen, Q. Tang, B. He, L. Lin, L. Yu, Platinum-free binary Co-Ni alloy counter electrodes for efficient dye-sensitized solar cells, Angew Chem Int Ed 53 (2014) 10799–10803.

[33] P.P. Das, A. Roy, M. Tathavadekar, P. SujathaDevi, Photovoltaic and photocatalytic performance of electrospun Zn2SnO4 hollow fibers, Appl. Catal. B 203 (2017) 692–703.

[34] L. Kavan, Electrochemistry and dye-sensitized solar cells, Curr. Opin. Electrochem. 2 (2017) 88–96.

[35] L. Kavan, J.-H. Yum, M. Graetzel, Graphene-based cathodes for liquid-junction dye sensitized solar cells: electrocatalytic and mass transport effects, Electrochim. Acta 128 (2014) 349–359.

[36] L. Kavan, P. Liska, S.M. Zakeeruddin, M. Grätzel, Low-temperature fabrication of highly-efficient, optically-transparent (FTO-free) graphene cathode for Co-mediated dye-sensitized solar cells with acetonitrile-free electrolyte solution, Electrochim. Acta 195 (2016) 34–42.

[37] L. Kavan, H. Krysova, P. Janda, H. Tarabkova, Y. Saygili, M. Freitag, S.M. Zakeeruddin, A. Hagfeldt, M. Grätzel, Novel highly active Pt/graphene catalyst for cathodes of Cu(II/I)-mediated dye-sensitized solar cells, Electrochim. Acta 251 (2017) 167–175.

[38] M. Janani, P. Srikrishnarka, S.V. Nair, A.S. Nair, An in-depth review on the role of carbon nanostructures in dye-sensitized solar cells, J. Mater. Chem. A 3 (2015) 17914–17938.

[39] L. Kavan, J.H. Yum, M. Grätzel, Optically transparent cathode for dye-sensitized solar cells based on graphene nanoplatelets, ACS Nano 5 (2010) 165–172.

[40] W. Yang, X. Xu, Y. Gao, Z. Li, C. Li, W. Wang, Y. Chen, G. Ning, L. Zhang, F. Yang, S. Chen, A. Wang, J. Kong, Y. Li, High-surface-area nanomesh graphene with enriched edge sites as efficient metal-free cathodes for dye-sensitized solar cells, Nanoscale 8 (2016) 13059–13066.

[41] J.M. Rhodes, C.A. Jones, L.B. Thal, J.E. Macdonald, Phase-controlled colloidal syntheses of iron sulfide nanocrystals via sulfur precursor reactivity and direct pyrite precipitation, Chem. Mater. 29 (2017) 8521–8530.

[42] P. Kulkarni, S.K. Nataraj, R.G. Balakrishna, D.H. Nagaraju, M.V. Reddy, Nanostructured binary and ternary metal sulfides: synthesis methods and their application in energy conversion and storage devices, J. Mater. Chem. A Mater. Energy Sustain. 5 (2017) 22040–22094.

[43] J. Yao, K. Zhang, W. Wang, X. Zuo, Q. Yang, H. Tang, M. Wu, G. Li, Functional integration and self-template synthesis of hollow core-shell carbon mesoporous spheres/Fe$_3$O$_4$/nitrogen-doped graphene to enhance catalytic activity in DSSCs, Nanoscale 10 (2018) 7946–7956.

[44] F. Gong, H. Wang, X. Xu, G. Zhou, Z.S. Wang, In situ growth of Co$_{(0.85)}$Se and Ni$_{(0.85)}$Se on conductive substrates as high-performance counter electrodes for dye-sensitized solar cells, J. Am. Chem. Soc. 134 (2012) 10953–10958.

[45] Y. Hou, D. Wang, X.H. Yang, W.Q. Fang, B. Zhang, H.F. Wang, G.Z. Lu, P. Hu, H.J. Zhao, H.G. Yang, Rational screening low-cost counter electrodes for dye-sensitized solar cells, Nat. Commun. 4 (2013) 1583.

[46] H. Zhang, Y. Wang, P. Liu, S.L. Chou, J.Z. Wang, H. Liu, G. Wang, H. Zhao, Highly ordered single crystalline nanowire array assembled three-dimensional Nb$_3$O$_7$(OH) and Nb$_2$O$_5$ superstructures for energy storage and conversion applications, ACS Nano 10 (2016) 507–514.

[47] H. Wang, G. Liu, X. Li, P. Xiang, Z. Ku, Y. Rong, M. Xu, L. Liu, M. Hu, Y. Yang, H. Han, Highly efficient poly(3-hexylthiophene) based monolithic dye-sensitized solar cells with carbon counter electrode, Energy Environ. Sci. 4 (2011).

[48] J. Kwon, V. Ganapathy, Y.H. Kim, K.D. Song, H.G. Park, Y. Jun, P.J. Yoo, J.H. Park, Nanopatterned conductive polymer films as a Pt, TCO-free counter electrode for low-cost dye-sensitized solar cells, Nanoscale 5 (2013) 7838–7843.

[49] F. Yu, Z. Wang, S. Zhang, K. Yun, H. Ye, X. Gong, H. Tian, N-Annulated perylene-based organic dyes sensitized graphitic carbon nitride to form an amide bond for efficient photocatalytic hydrogen production under visible-light irradiation, Appl. Catal. B 5 (2018) 32–42.

[50] H. Hu, Bu Y. Guan, Xiong W. Lou, Construction of complex CoS hollow structures with enhanced electrochemical properties for hybrid supercapacitors, Chem 1 (2016) 102–113.

[51] L. Shen, L. Yu, X.Y. Yu, X. Zhang, X.W. Lou, Self-templated formation of uniform NiCo$_2$O$_4$ hollow spheres with complex interior structures for lithium-ion batteries

and supercapacitors, Angew Chem Int Ed 54 (2015) 1868–1872.

[52] G. Zhan, H.C. Zeng, Hydrogen spillover through Matryoshka-type (ZIFs@)n-1ZIFs nanocubes, Nat. Commun. 9 (2018) 3778.

[53] B. Sun, X. Feng, Y. Yao, Q. Su, W. Ji, C.-T. Au, Substantial pretreatment effect on CO oxidation over controllably synthesized Au/FeOx hollow nanostructures via hybrid Au/β-FeOOH@SiO$_2$, ACS Catal. 3 (2013) 3099–3105.

[54] F.X. Ma, H. Hu, H.B. Wu, C.Y. Xu, Z. Xu, L. Zhen, X.W. David Lou, Formation of uniform Fe$_3$O$_4$ hollow spheres organized by ultrathin nanosheets and their excellent Lithium storage properties, Adv Mater 27 (2015) 4097–4101.

[55] L. Shang, H. Yu, X. Huang, T. Bian, R. Shi, Y. Zhao, G.I. Waterhouse, L.Z. Wu, C.H. Tung, T. Zhang, Well-dispersed ZIF-derived Co, N-Co-doped carbon nanoframes through mesoporous-silica-protected calcination as efficient oxygen reduction electrocatalysts, Adv Mater 28 (2016) 1668–1674.

[56] C. Wang, F. Wang, Z. Liu, Y. Zhao, Y. Liu, Q. Yue, H. Zhu, Y. Deng, Y. Wu, D. Zhao, N-doped carbon hollow microspheres for metal-free quasi-solid-state full sodium-ion capacitors, Nano Energy 41 (2017) 674–680.

[57] D.S. Bin, Z.X. Chi, Y. Li, K. Zhang, X. Yang, Y.G. Sun, J.Y. Piao, A.M. Cao, L.J. Wan, Controlling the compositional chemistry in single nanoparticles for functional hollow carbon nanospheres, J. Am. Chem. Soc. 139 (2017) 13492–13498.

[58] M. Idrees, S. Batool, J. Kong, Q. Zhuang, H. Liu, Q. Shao, N. Lu, Y. Feng, E.K. Wujcik, Q. Gao, T. Ding, R. Wei, Z. Guo, Polyborosilazane derived ceramics - Nitrogen sulfur dual doped graphene nanocomposite anode for enhanced lithium ion batteries, Electrochim. Acta 296 (2019) 925–937.

[59] W. Du, X. Wang, J. Zhan, X. Sun, L. Kang, F. Jiang, X. Zhang, Q. Shao, M. Dong, H. Liu, V. Murugadoss, Z. Guo, Biological cell template synthesis of nitrogen-doped porous hollow carbon spheres/MnO$_2$ composites for high-performance asymmetric supercapacitors, Electrochim. Acta 296 (2019) 907–915.

[60] J. Chen, X. Wang, Y. Huang, S. Lv, X. Cao, J. Yun, D. Cao, Adsorption removal of pollutant dyes in wastewater by nitrogen-doped porous carbons derived from natural leaves, Eng. Sci. 5 (2019) 30–38.

[61] H. Qi, M. Teng, M. Liu, S. Liu, J. Li, H. Yu, C. Teng, Z. Huang, H. Liu, Q. Shao, A. Umar, T. Ding, Q. Gao, Z. Guo, Biomass-derived nitrogen-doped carbon quantum dots: highly selective fluorescent probe for detecting Fe$^{(3+)}$ ions and tetracyclines, J. Colloid Interface Sci. 539 (2019) 332–341.

[62] T. Liu, C. Jiang, B. Cheng, W. You, J. Yu, Hierarchical NiS/N-doped carbon composite hollow spheres with excellent supercapacitor performance, J. Mater. Chem. A Mater. Energy Sustain. 5 (2017) 21257–21265.

[63] S.-L. Jian, Y.-J. Huang, M.-H. Yeh, K.-C. Ho, A zeolitic imidazolate framework-derived ZnSe/N-doped carbon cube hybrid electrocatalyst as the counter electrode for dye-sensitized solar cells, J. Mater. Chem. A 6 (2018) 5107–5118.

[64] X. Meng, C. Yu, X. Song, Y. Liu, S. Liang, Z. Liu, C. Hao, J. Qiu, Nitrogen-doped graphene nanoribbons with surface enriched active sites and enhanced performance for dye-sensitized solar cells, Adv. Energy Mater. 5 (2015).

[65] F. Du, X. Zuo, Q. Yang, G. Li, Z. Ding, M. Wu, Y. Ma, K. Zhu, Nanohybrids of RGO nanosheets and 2-dimensional porous Co3O4 nanoflakes working as highly efficient counter electrodes for dye-sensitized solar cells, J. Mater. Chem. C 4 (2016) 10323–10328.

[66] C. Yang, M.Y. Gao, Q.B. Zhang, J.R. Zeng, X.T. Li, A.P. Abbott, In-situ activation of self-supported 3D hierarchically porous Ni3S2 films grown on nanoporous copper as excellent pH-universal electrocatalysts for hydrogen evolution reaction, Nano Energy 36 (2017) 85–94.

[67] X. Meng, C. Yu, X. Zhang, L. Huang, M. Rager, J. Hong, J. Qiu, Z. Lin, Active sites-enriched carbon matrix enables efficient triiodide reduction in dye-sensitized solar cells: an understanding of the active centers, Nano Energy 54 (2018) 138–147.

[68] Y.Z. Chen, C. Wang, Z.Y. Wu, Y. Xiong, Q. Xu, S.H. Yu, H.L. Jiang, From bimetallic metal-organic framework to porous carbon: high surface area and multicomponent active dopants for excellent electrocatalysis, Adv Mater 27 (2015) 5010–5016.

[69] S. Liu, Z. Wang, S. Zhou, F. Yu, M. Yu, C.Y. Chiang, W. Zhou, J. Zhao, J. Qiu, Metal-

organic-Framework-Derived hybrid carbon nanocages as a bifunctional electrocatalyst for oxygen reduction and evolution, Adv Mater 29 (2017).

[70] D. Guo, Xa. Chen, H. Wei, M. Liu, F. Ding, Z. Yang, et al., Controllable synthesis of highly uniform flower-like hierarchical carbon nanospheres and their application in high performance lithium–sulfur batteries, J. Mater. Chem. A 5 (2017) 6245–6256.

[71] M. Guo, B. Tang, H. Zhang, S. Yin, W. Jiang, Y. Zhang, M. Li, H. Wang, L. Jiao, A high efficiency CoCr$_{(2)}$O$_{(4)}$/carbon nanotubes nanocomposite electrocatalyst for dye-sensitised solar cells, Chem. Commun. (Camb.) 50 (2014) 7356–7358.

[72] S.K. Swami, N. Chaturvedi, A. Kumar, R. Kapoor, V. Dutta, J. Frey, T. Moehl, M. Grätzel, S. Mathew, M.K. Nazeeruddin, Investigation of electrodeposited cobalt sulphide counter electrodes and their application in next-generation dye sensitized solar cells featuring organic dyes and cobalt-based redox electrolytes, J. Power Sources 275 (2015) 80–89.

[73] F. Liu, J. Zhu, L. Hu, B. Zhang, J. Yao, M.K. Nazeeruddin, M. Grätzel, S. Dai, Low-temperature, solution-deposited metal chalcogenide films as highly efficient counter electrodes for sensitized solar cells, J. Mater. Chem. A 3 (2015) 6315–6323.

[74] J. Yao, Z. Zhang, W. Wang, X. Zuo, Q. Yang, M. Wu, G. Li, Great enhancement of electrochemical cyclic voltammetry stabilization of Fe$_3$O$_4$ microspheres by introducing 3DRGO, Electrochim. Acta 279 (2018) 168–176.

[75] D.H. Kweon, J.B. Baek, Edge-functionalized graphene nanoplatelets as metal-free electrocatalysts for dye-sensitized solar cells, Adv Mater 31 (2019) 1804440.

[76] X. Meng, C. Yu, X. Song, J. Iocozzia, J. Hong, M. Rager, H. Jin, S. Wang, L. Huang, J. Qiu, Z. Lin, Scrutinizing defects and defect density of selenium-doped graphene for high-efficiency triiodide reduction in dye-sensitized solar cells, Angew. Chem. Int. Ed 57 (2018) 4682–4686.

[77] Y. Niu, X. Qian, J. Zhang, W. Wu, H. Liu, C. Xu, L. Hou, Stepwise synthesis of CoS$_2$-C@CoS$_2$ yolk-shell nanocages with much enhanced electrocatalytic performances both in solar cells and hydrogen evolution reactions, J. Mater. Chem. A 6 (2018) 12056–12065.

[78] B. Yang, X. Zuo, P. Chen, L. Zhou, X. Yang, H. Zhang, G. Li, M. Wu, Y. Ma, S. Jin, X. Chen, Nanocomposite of tin sulfide nanoparticles with reduced graphene oxide in high-efficiency dye-sensitized solar cells, ACS Appl. Mater. Interfaces 7 (2015) 137–143.

[79] C. Yu, X. Meng, X. Song, S. Liang, Q. Dong, G. Wang, C. Hao, X. Yang, T. Ma, P.M. Ajayan, J. Qiu, Graphene-mediated highly-dispersed MoS$_2$ nanosheets with enhanced triiodide reduction activity for dye-sensitized solar cells, Carbon 100 (2016) 474–483.

[80] S.-W. Yoon, V.-D. Dao, L.L. Larina, J.-K. Lee, H.-S. Choi, Optimum strategy for designing PtCo alloy/reduced graphene oxide nanohybrid counter electrode for dye-sensitized solar cells, Carbon 96 (2016) 229–236.

[81] A. Shrestha, M. Batmunkh, C.J. Shearer, Y. Yin, G.G. Andersson, J.G. Shapter, S. Qiao, S. Dai, Nitrogen-doped CN$_x$/CNTs heteroelectrocatalysts for highly efficient dye-sensitized solar cells, Adv. Energy Mater. 7 (2017).

[82] Y. Ma, J. Huang, L. Lin, Q. Xie, M. Yan, B. Qu, L. Wang, L. Mai, D.-L. Peng, Self-assembly synthesis of 3D graphene-encapsulated hierarchical Fe$_3$O$_4$ nano-flower architecture with high lithium storage capacity and excellent rate capability, J. Power Sources 365 (2017) 98–108.

[83] P. Zhai, C.-C. Lee, Y.-H. Chang, C. Liu, T.-C. Wei, S.-P. Feng, A significant improvement in the electrocatalytic stability of N-Doped graphene nanosheets used as a counter electrode for [Co(bpy)$_3$]$^{3+/2+}$ based porphyrin-sensitized solar cells, ACS Appl. Mater. Interfaces 7 (2015) 2116–2123.

[84] H. Jiang, Y. Lin, B. Chen, Y. Zhang, H. Liu, X. Duan, D. Chen, L. Song, Ternary interfacial superstructure enabling extraordinary hydrogen evolution electrocatalysis, Mater. Today 21 (2018) 602–610.

[85] X. Meng, C. Yu, X. Song, Z. Liu, B. Lu, C. Hao, J. Qiu, Rational design and fabrication of sulfur-doped porous graphene with enhanced performance as a counter electrode in dye-sensitized solar cells, J. Mater. Chem. A 5 (2017) 2280–2287.